

Upstanding Rashba spin in honeycomb lattices: Electrically reversible surface spin polarization

Ming-Hao Liu^{1,2,*} and Ching-Ray Chang^{1,†}

¹Department of Physics, National Taiwan University, Taipei 10617, Taiwan

²Center for Quantum Science and Engineering (CQSE), National Taiwan University, Taipei 10617, Taiwan

(Dated: November 14, 2018)

The spin-split states subject to Rashba spin-orbit coupling in two-dimensional systems have long been accepted as pointing inplane and perpendicular to the corresponding wave vectors. This is in general true for free-electron model, but exceptions do exist elsewhere. Within the tight-binding model, we unveil the unusual upstanding behavior of those Rashba spins around \bar{K} and \bar{K}' points in honeycomb lattices. Our calculation (i) explains the recent experiment of the $\text{Ti/Si(111)-(1} \times 1\text{)}$ surface alloy [K. Sakamoto *et al.*, Phys. Rev. Lett. **102**, 096805 (2009)], where abrupt upstanding spin states near \bar{K} are observed, and (ii) predicts an electrically reversible out-of-plane surface spin polarization.

PACS numbers: 73.20.At, 73.63.-b, 71.70.Ej

The honeycomb lattice is one of the three types of two-dimensional regular tessellation—triangular, square, and hexagonal tilings. In solid-state physics, the honeycomb lattice is described by two staggered triangular sublattices. The identity of the comprising atoms of the two sublattices determines if the honeycomb is monoatomic or diatomic, and their interlayer distance determines whether the honeycomb is flat or bilayer. Thus graphene and boron nitride are monoatomic and diatomic flat honeycombs, respectively,¹ Bi(111) bilayer surface² is a monoatomic bilayer honeycomb, and $\text{Ti/Si(111)-(1} \times 1\text{)}$ surface alloy³ is a diatomic bilayer honeycomb.

Among these honeycomb lattices, graphene has been under the most intensive investigation due to its unusual Dirac-like electronic excitations.⁴ When deposited on a substrate, the structural inversion symmetry perpendicular to the graphene plane is broken, and the Rashba spin-orbit coupling⁵ hence emerges. Recent experimental measurement of Rashba spin splitting in graphene on Ni(111) substrate with⁶ and without⁷ an intercalated Au monolayer eventually drew theorists' attention to the electronic structure, in the presence of Rashba coupling, of graphene,⁸ i.e., near \bar{K} and \bar{K}' in monoatomic flat honeycomb. In other honeycomb systems, Bi(111) bilayer surface is believed to contain strong Rashba coupling⁹ and exhibit interesting spin-Hall patterns,¹⁰ and a more recent experimental effort even shows an unusual Rashba spin behavior at \bar{K} point in $\text{Ti/Si(111)-(1} \times 1\text{)}$ surface alloy.³

In this Rapid Communication we present a unified tight-binding description to understand the Rashba effect in honeycomb lattices. To focus on the major effect brought by the Rashba coupling, we consider electron hopping up to the nearest neighbors. Particular attention will be paid to the spin configuration near \bar{K} and \bar{K}' points, which shows an abrupt upstanding Rashba spin behavior, in good agreement with Ref. 3. Moreover, we show that the upstanding spins along \bar{K} and \bar{K}' directions are opposite. Accordingly, we propose an electrically reversible out-of-plane surface polarization, which will be numerically shown by Landauer-Keldysh formalism.

Consider a honeycomb lattice constructed by primitive translation vectors $\mathbf{t}_1 = a(1/2, \sqrt{3}/2, 0)$ and $\mathbf{t}_2 = a(-1/2, \sqrt{3}/2, 0)$, and basis vectors $\mathbf{d}_1 = 0$ and $\mathbf{d}_2 = a(0, 1/\sqrt{3}, d_z)$, where a is the lattice constant. For flat honey-

combs we have $d_z = 0$, and $d_z \neq 0$ describes a bilayer case. We begin with the 4×4 tight-binding Hamiltonian¹⁰ of the Slater and Koster type,^{1,11}

$$\mathbb{H} = \begin{pmatrix} \mathbb{H}_{11} & \mathbb{H}_{12} \\ \mathbb{H}_{12}^\dagger & \mathbb{H}_{22} \end{pmatrix}, \quad (1)$$

with off-diagonal element

$$\mathbb{H}_{12} = \begin{pmatrix} U(1+2F) & -it_R(1-F-\sqrt{3}G) \\ -it_R(1-F+\sqrt{3}G) & U(1+2F) \end{pmatrix}, \quad (2)$$

where t_R is the Rashba hopping strength, $U \equiv l_z^2 V_{pp\sigma} + (1-l_z^2) V_{pp\pi}$, l_z being the direction cosine of nearest neighbors ($l_z = 0$ for flat and $l_z \neq 0$ for bilayer), is the two-center interaction integral involving p_z atomic orbitals, and the compact functions are given by $F \equiv \exp(-i\sqrt{3}k_y a/2) \cos(k_x a/2)$ and $G \equiv \exp(-i\sqrt{3}k_y a/2) \sin(k_x a/2)$. The diagonal elements of Eq. (1) are $\mathbb{H}_{ii} = E_{pi} \mathbb{I}$ with \mathbb{I} the 2×2 identity matrix and $i = 1, 2$. For monoatomic honeycombs, we have $E_{p1} = E_{p2} = E_p$ but for diatomic honeycombs, $E_{p1} \neq E_{p2}$. In the following we consider $E_{p1} = E_{p2}$; straightforward generalization to the diatomic case will be shown later.

Adopting the same trick of Rashba,⁸ Eq. (1) can be reduced to a 2×2 Hamiltonian,

$$\mathbb{H}_A(E) = E_p \mathbb{I} + \frac{\mathbb{H}_{12} \mathbb{H}_{12}^\dagger}{E - E_p} \quad (3)$$

for sublattice A , which depends explicitly on its eigenvalue E . The Schrödinger equation of Hamiltonian (3) is $\mathbb{H}_A(E) |\psi_A\rangle = E |\psi_A\rangle$. By solving the characteristic equation $\det(\mathbb{H}_A(E) - E) = 0$ the eigenvalues of Eq. (3) can be written as

$$E_{\mu\nu} = E_p + \mu E_\nu, \quad \mu, \nu = \pm 1 \quad (4)$$

with

$$E_\nu = \sqrt{\frac{\text{Tr } h + \nu \sqrt{(\text{Tr } h)^2 - 4 \det h}}{2}}, \quad (5)$$

where

$$h = \mathbb{H}_{12}\mathbb{H}_{12}^\dagger = \begin{pmatrix} h_{11} & h_{12} \\ h_{21} & h_{22} \end{pmatrix} \quad (6)$$

will play an important role in the following derivation. The eigenvectors can be written as either of

$$|\psi_A^{\mu\nu}\rangle = \left(|h_{12}|^2 + |E_\nu^2 - h_{11}|^2\right)^{-1/2} \begin{pmatrix} h_{12} \\ E_\nu^2 - h_{11} \end{pmatrix} \quad (7a)$$

$$|\psi_A^{\mu\nu}\rangle = \left(|E_\nu^2 - h_{22}|^2 + |h_{21}|^2\right)^{-1/2} \begin{pmatrix} E_\nu^2 - h_{22} \\ h_{21} \end{pmatrix}, \quad (7b)$$

which are independent of μ . Both Eqs. (7a) and (7b) are valid for carrying out the spin expectation $\langle \vec{S} \rangle = (\hbar/2)\langle \vec{\sigma} \rangle$, $\vec{\sigma} = (\sigma^x, \sigma^y, \sigma^z)$ being the Pauli matrix vector, except at the symmetry points $\bar{\Gamma}$, \bar{M} , \bar{K} and \bar{K}' . With careful treatment at those points, the spin direction $\langle \vec{S} \rangle_{\mu\nu} = (\hbar/2)\langle \psi_A^{\mu\nu} | \vec{\sigma} | \psi_A^{\mu\nu} \rangle$ based on Eq. (7) subject to the four eigenstate branches are shown in Figs. 1(a)–1(c); the band structure according to Eqs. (2)–(6) is shown in Fig. 1(d). Clearly one can see an abrupt upstanding component $\langle S_z \rangle_{\mu\nu}$ near \bar{K} and \bar{K}' points. For the $\nu = +1$ branch, we depict the spin configuration based on Eq. (7) in Fig. 2, where each arrow is determined by $(\langle \sigma^x \rangle_{\mu+}, \langle \sigma^y \rangle_{\mu+})$ and the color shading is by $\langle \sigma^z \rangle_{\mu+}$. The bright (dark) region of $\langle \sigma^z \rangle \approx 1$ ($\langle \sigma^z \rangle \approx -1$) around \bar{K} (\bar{K}') can be clearly seen in the main panel of Fig. 2, reflecting its inherent C_3 symmetry.

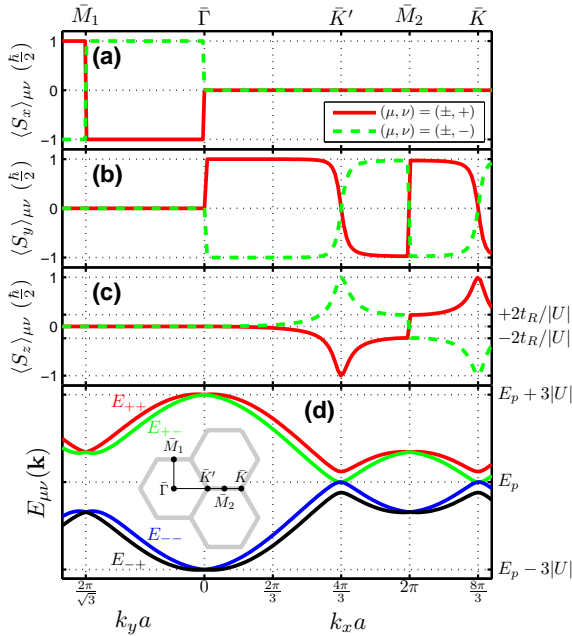


FIG. 1: (Online color) The spin components (a) $\langle S_x \rangle_{\mu\nu}$, (b) $\langle S_y \rangle_{\mu\nu}$, and (c) $\langle S_z \rangle_{\mu\nu}$ of energy eigenstates of a Rashba spin-orbit-coupled monoatomic honeycomb lattice with its band structure shown in (d). The parameters are set $t_R/|U| = 0.12$. The Brillouin zone is shown in the inset in (d).

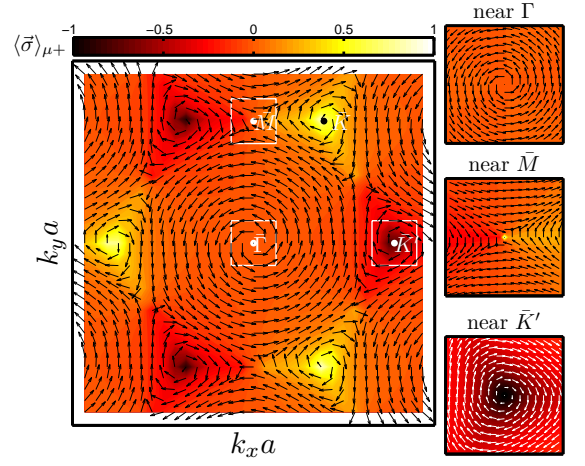


FIG. 2: (Color online) Spin configuration for the $\nu = +1$ branche. Each arrow is given by $(\langle \sigma^x \rangle_{\mu+}, \langle \sigma^y \rangle_{\mu+})$ and the color shading is determined by $\langle \sigma^z \rangle_{\mu+}$.

To provide deeper understanding of Fig. 1, as well as the zoomed-in plots of Fig. 2, below we give a series of discussion of $E_{\mu\nu}$ and $\langle \vec{\sigma} \rangle_{\mu\nu}$ around those symmetry points.

The $\bar{\Gamma}$ point. Assuming $\mathbf{k} = \vec{\delta} = \delta(\cos \phi, \sin \phi)$ with $\delta a \ll 1$, one can obtain

$$E_\nu(\bar{\Gamma} + \vec{\delta}) \approx 3|U| + \frac{(t_R^2 - 2U^2)}{8|U|} \delta^2 a^2 + \nu \frac{\sqrt{3}}{2} t_R \delta a \quad (8)$$

and $\langle \vec{\sigma} \rangle_{\mu\nu}(\bar{\Gamma} + \vec{\delta}) \approx -\nu(\sin \phi, -\cos \phi, 0)$ which is identical to the free-electron case. Equation (8) is useful for determining parameters E_p , U , and t_R by matching with the free-electron dispersion $E(k) = E_0 + \hbar^2 k^2 / 2m^* \pm \alpha k$. The band offset E_0 , the Rashba parameter α , and the curvature $\hbar^2 / 2m^*$ (or the effective mass m^*), as well as the lattice constant a are experimentally measurable. In the usual $t_R^2 \ll |U|^2$ case we have $E_p = E_0 + |3U|$, $|U| = 2\hbar^2 / m^* a^2$, and $t_R = 2\alpha / \sqrt{3}a$.

The \bar{M} point. Let $\bar{M} = (2\pi/a, 0)$, i.e., \bar{M}_2 in Fig. 1. Assuming $\mathbf{k} = \bar{M} + \vec{\delta} = (2\pi/a + \delta_x, \delta_y)$ one obtains an anisotropically free-electron-like dispersion,

$$E_\nu(\bar{M} + \vec{\delta}) \approx \sqrt{U^2 + 4t_R^2} - \frac{|U|}{4} (\delta_x^2 - 3\delta_y^2) a^2 + \nu \frac{\sqrt{3}}{2} t_R \sqrt{\delta_x^2 + 9\delta_y^2} a, \quad (9)$$

which indicates that \bar{M} is a saddle point as one can see from the different sign of δ_x^2 and δ_y^2 in the second term. This means that the effective mass of the electron at state near \bar{M} has opposite sign when going *along* and *perpendicular* to the Brillouin-zone boundary. In addition, the latter has an effective mass 3 times lighter and an effective Rashba parameter three times stronger than the former. Equation (9) therefore explains why we have band shape near $\bar{\Gamma}$ identical with that near \bar{M}_2 but not \bar{M}_1 [see Fig. 1(d)].

The anisotropy at \bar{M} also reveals in the corresponding spin

direction,

$$\langle \vec{\sigma} \rangle_{\mu\nu}(\bar{M} + \vec{\delta}) \approx \frac{\nu}{\sqrt{5 - 4\cos 2\phi}} \begin{pmatrix} 3\sin\phi \\ \cos\phi \\ \frac{2t_R}{|U|}\cos\phi \end{pmatrix}, \quad (10)$$

where we keep terms up to first order in $t_R/|U|$. Clearly from Eq. (10) the z component saturates to $2t_R/|U|$ along the Brillouin boundary near \bar{M} but vanishes when going perpendicular to the boundary [see Fig. 1(c)].

The \bar{K} and \bar{K}' points. Let $\bar{K}' = (\mathbf{g}_1 - \mathbf{g}_2)/3$. Assuming $\mathbf{k} = \bar{K}' + \vec{\delta} = (4\pi/3a + \delta_x, 0 + \delta_y)$ we obtain

$$E_\nu(\bar{K}' + \vec{\delta}) \approx \frac{1}{2} \sqrt{(3t_R)^2 + 3U^2\delta^2a^2} + \nu \frac{3t_R}{2}, \quad (11)$$

in agreement with Ref. 8. The spin direction near \bar{K}' , up to second order in (δa) , is given by

$$\langle \vec{\sigma} \rangle_{\mu\nu}(\bar{K}' + \vec{\delta}) = \nu \begin{pmatrix} -\frac{U}{\sqrt{3}t_R}\delta a \sin\phi \\ \frac{U}{\sqrt{3}t_R}\delta a \cos\phi \\ -1 + \frac{1}{6}\frac{U^2}{t_R^2}\delta^2a^2 \end{pmatrix}, \quad (12)$$

which shows at \bar{K}' we have $\langle \sigma^z \rangle_{\mu\pm}(\bar{K}') = \mp 1$. Around \bar{K} the dispersion is identical to Eq. (11), and the spin configuration has a reversed helicity, i.e., opposite out-of-plane component,

$$\langle \sigma^z \rangle_{\mu\nu}(\bar{K} + \vec{\delta}) = -\langle \sigma^z \rangle_{\mu\nu}(\bar{K}' + \vec{\delta}), \quad (13)$$

but unchanged inplane component.

So far the discussion is basically for sublattice A since we have obtained reduced Hamiltonian (3) by expressing the wave function of sublattice B , ψ_B , in terms of that of sublattice A , ψ_A . We could have as well expressed ψ_A in terms of ψ_B ; the resulting reduced Hamiltonian then would be $\mathbb{H}_B(E) = E_p\mathbb{I} + \mathbb{H}_{12}^\dagger/(E - E_p)$, leading to identical dispersion, identical inplane spin direction, but opposite $\langle \sigma^z \rangle$ component,

$$\langle \psi_A | \sigma^z | \psi_A \rangle = -\langle \psi_B | \sigma^z | \psi_B \rangle. \quad (14)$$

In addition, we have so far focused on the monoatomic honeycomb lattice. For different sublattice atoms A and B , we have $E_{p1} \neq E_{p2}$. The energy dispersion can be straightforwardly derived as $\varepsilon_{\mu\nu}(\mathbf{k}) = \bar{E}_p + \mu\varepsilon_\nu$ with $\varepsilon_\nu = \sqrt{\Delta_p^2 + E_\nu^2}$, $\bar{E}_p = (E_{p1} + E_{p2})/2$, $\Delta_p = (E_{p1} - E_{p2})/2$, and E_ν given by Eq. (5). Noticing from Eqs. (8), (9), and (11) that around the symmetry points $E_+ \neq E_-$ occurs only at \bar{K} and \bar{K}' , we expect the modification to the band structure due to Δ_p appears the most salient at \bar{K} and \bar{K}' . Indeed, with $E_\nu(\mathbf{k} = \bar{K} \text{ or } \bar{K}') = 3t_R(1 + \nu)/2$ a gap $\varepsilon_{+-} - \varepsilon_{--} = 2\varepsilon_- = 2|\Delta_p|$ is opened. At other symmetry points, $\varepsilon_{\mu\pm}$ remain degenerate. Despite the opened gap, however, the eigenvectors surprisingly remain the same as Eq. (7), and the upstanding Rashba

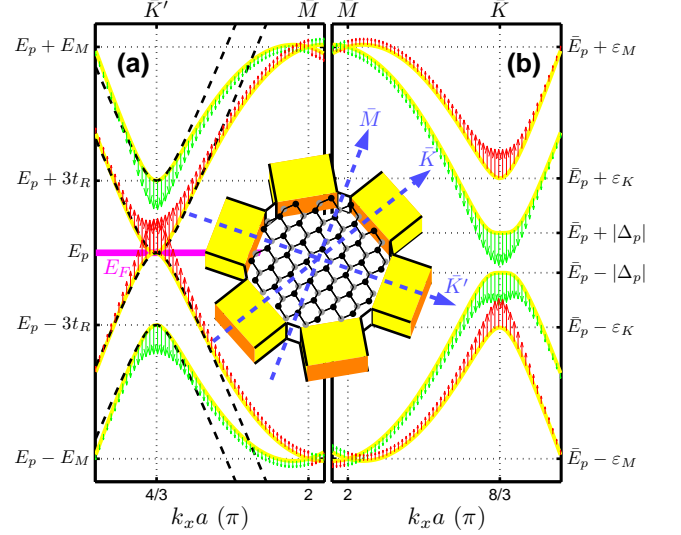


FIG. 3: (Color online) Energy dispersion and $\langle \sigma^z \rangle_{\mu\nu}$ (indicated by arrows) for (a) monoatomic and (b) diatomic honeycomb lattices. In (a) the black dashed lines are the approximated dispersions given by Eq. (11); $E_M = \sqrt{U^2 + 4t_R^2}$. In (b) we set $\Delta_p = 0.1|U|$; $\varepsilon_M = \sqrt{\Delta_p^2 + U^2 + 4t_R^2}$ and $\varepsilon_K = \sqrt{\Delta_p^2 + (3t_R)^2}$. The inset shows a six-terminal bilayer honeycomb channel with black (gray) dots the upper (lower) sublattice.

spin around \bar{K} and \bar{K}' described previously is therefore unchanged.

To show the opened gap with unchanged spin direction, we plot the energy dispersion curves with $\langle \sigma^z \rangle_{\mu\nu}$ in Fig. 3 for monoatomic honeycomb near \bar{K}' [panel (a)] and diatomic honeycomb near \bar{K} [panel (b)]. Figure 3(b) readily explains the recent spin-resolved angle-resolved photoelectron spectroscopy data for the Tl/Si(111)-(1 × 1) surface alloy.³ In such surface alloy,^{12,13} the Tl coverage on the Si(111) substrate is one monolayer, and the topmost Tl (sublattice A) and Si (sublattice B) layers form a diatomic honeycomb lattice of the bilayer type ($d_z < 0$). The $\mu = +1$ branch in Fig. 3(b) thus resembles the band feature near \bar{K} reported in Ref. 3. It is important to note, however, that for flat honeycombs such as graphene, both sublattices A and B will be simultaneously measured, leading to vanishing $\langle S_z \rangle$, in view of Eq. (14).

We have shown that the upstanding Rashba spin around \bar{K} and \bar{K}' points is a fundamental property of the spin configuration in honeycomb lattices, whether flat or bilayer, monoatomic or diatomic. Next we illustrate how striking this property can be. For simplicity, let us consider a six-terminal channel made of monoatomic bilayer honeycomb. See the inset in Fig. 3. Assume that the transport of this six-terminal device is supported by the surface states so that electrons are only allowed to hop within the surface bilayer, i.e., the honeycomb lattice. Let the Fermi energy E_F lie just at E_p . The situation is like Fig. 3(a). Recalling Eq. (14) we expect that when driving the electrons along \bar{K}' , the transport states with $E_F = E_p$ are $+z$ spin polarized on sublattice A but $-z$ spin polarized on sublattice B . Recalling further Eq. (13), the sur-

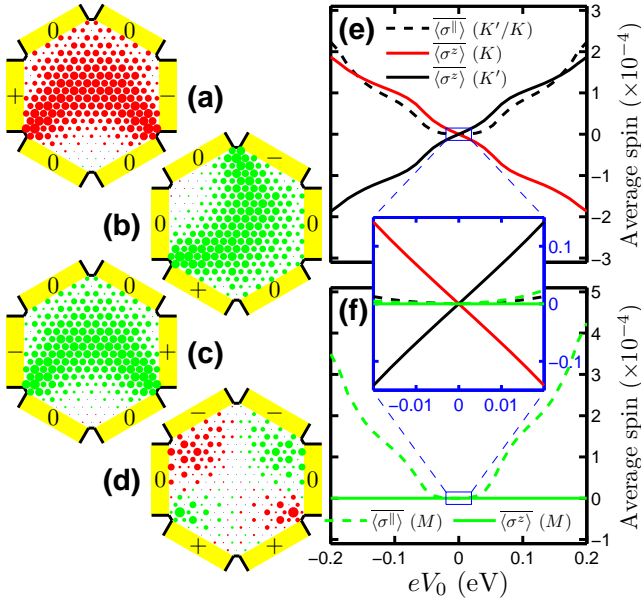


FIG. 4: (Online color) Surface spin polarization in a 6-terminal bilayer honeycomb channel with (a) \bar{K}' biasing, (b) and (c) \bar{K} biasing, and (d) \bar{M} biasing. Red/gray (green/light gray) dots represent a $\langle \sigma^z \rangle > 0$ ($\langle \sigma^z \rangle < 0$) local spin density with the dot size proportional to $|\langle \sigma^z \rangle|$. $\langle \sigma^z \rangle$ and $\langle \sigma_{\parallel} \rangle$ as functions of the bias eV_0 are shown in (e) for \bar{K}/\bar{K}' biasing and in (f) for \bar{M} biasing.

face spin polarization (assumed to be contributed by sublattice A only) is out-of-plane and can be electrically controlled by either \bar{K} or \bar{K}' biasing.

To visualize this idea, let us calculate for the six-terminal bilayer honeycomb channel the local spin densities by employing the Landauer-Keldysh^{14,15} formalism, subject to Hamiltonian, $\mathcal{H} = E_p \sum_n c_n^\dagger c_n + \sum_{\langle nm \rangle} c_m^\dagger [U\mathbb{I} + it_R(\vec{\sigma} \times \mathbf{d}_{mn})_z] c_n$, with c_n^\dagger (c_n) the creation (annihilation) operator of the electron on site n and \mathbf{d}_{mn} the unit vector pointing from site n to m . The total number of lattice sites in the honeycomb channel is 480. For clarity we will plot $\langle \sigma^z \rangle$ only on

the surface (sublattice A). A positive (negative) $\langle \sigma^z \rangle$ on each site will be denoted by a red (green) dot, with the dot size proportional to the magnitude of $\langle \sigma^z \rangle$. The applied potential energy of $\pm eV_0/2$ will be denoted as “ \pm ,” and $eV_0 = 0$ as “0” on each lead. The parameters $E_p = 0$, $U = -1$ eV, and $t_R/|U| = 0.12$ are identical to those used in previous figures, and are within a realistic range.¹⁶ The bias is $eV_0 = 2$ meV.

First we drive the electrons from left to right, corresponding to \bar{K}' . As expected, we have a positive average of surface spin polarization $\langle \sigma^z \rangle > 0$, as shown in Fig. 4(a). When rotating the bias direction by 60° counterclockwise, the surface polarization becomes $\langle \sigma^z \rangle < 0$ as a consequence of Eq. (13) [see Fig. 4(b)]. Reversing the bias of Fig. 4(a) also switches \bar{K}' states to \bar{K} , leading to $\langle \sigma^z \rangle < 0$, as shown in Fig. 4(c). In Fig. 4(d) we drive the electrons from bottom to top, corresponding to the \bar{M} direction. The spin density distribution becomes completely different and satisfies the intrinsic spin-Hall symmetry, which yields $\langle \sigma^z \rangle = 0$. Figures 4(a) and 4(c) imply that the out-of-plane surface spin polarization can be flipped simply by reversing the bias, which is also a direct consequence of time-reversal operation. To show this electrical control of surface spin, we plot $\langle \sigma^z \rangle$ and $\langle \sigma_{\parallel} \rangle \equiv (\langle \sigma^x \rangle^2 + \langle \sigma^y \rangle^2)^{1/2}$ as a function of the bias eV_0 in Figs. 4(e) and 4(f) for \bar{K}'/\bar{K} and \bar{M} biasing, respectively. Within the low bias regime [see the inset between Figs. 4(e) and 4(f)], $\langle \sigma^z \rangle$ for \bar{K}'/\bar{K} biasing grows with eV_0 linearly, while other components are either vanishing or relatively small.

In conclusion, we have presented a unified tight-binding description to understand the Rashba effect in graphene, as well as bilayer surfaces and surface alloys of the honeycomb structure. Our results explain the recently observed abrupt upstanding Rashba spin in $\text{Ti/Si}(111)-(1 \times 1)$ surface alloy around \bar{K} , and predict an electrically reversible out-of-plane surface spin polarization, which may serve as a storage mechanism for future spintronic devices.

Financial support of the Republic of China National Science Council (Grant No. NSC 98-2112-M-002-012-MY3) is gratefully acknowledged.

* Electronic address: mhlui@phys.ntu.edu.tw

† Electronic address: crchang@phys.ntu.edu.tw

¹ G. Grosso and G. P. Parravicini, *Solid State Physics* (Academic Press, New York, 2000).

² P. Hofmann, *Prog. Surf. Sci.* **81**, 191 (2006).

³ K. Sakamoto et al., *Phys. Rev. Lett.* **102**, 096805 (2009).

⁴ A. H. C. Neto, F. Guinea, N. M. R. Peres, K. S. Novoselov, and A. K. Geim, *Reviews of Modern Physics* **81**, 109 (2009).

⁵ Y. A. Bychkov and E. I. Rashba, *JETP Lett.* **39**, 78 (1984).

⁶ A. Varykhalov et al., *Phys. Rev. Lett.* **101**, 157601 (2008).

⁷ Y. S. Dedkov, M. Fonin, U. Rudiger, and C. Laubschat, *Phys. Rev. Lett.* **100**, 107602 (2008).

⁸ E. I. Rashba, *Phys. Rev. B* **79**, 161409(R) (2009).

⁹ Y. M. Koroteev, G. Bihlmayer, J. E. Gayone, E. V. Chulkov, S. Blügel, P. M. Echenique, and P. Hofmann, *Phys. Rev. Lett.* **93**, 046403 (2004).

¹⁰ M.-H. Liu, G. Bihlmayer, S. Blügel, and C.-R. Chang, *Phys. Rev.*

B **76**, 121301(R) (2007).

¹¹ J. C. Slater and G. F. Koster, *Phys. Rev.* **94**, 1498 (1954).

¹² S. S. Lee, H. J. Song, N. D. Kim, J. W. Chung, K. Kong, D. Ahn, H. Yi, B. D. Yu, and H. Tochiara, *Phys. Rev. B* **66**, 233312 (2002).

¹³ K. Sakamoto, P. E. J. Eriksson, S. Mizuno, N. Ueno, H. Tochiara, and R. I. G. Uhrberg, *Phys. Rev. B* **74**, 075335 (2006).

¹⁴ B. K. Nikolić, S. Souma, L. P. Zarbo, and J. Sinova, *Phys. Rev. Lett.* **95**, 046601 (2005).

¹⁵ B. K. Nikolić, L. P. Zarbo, and S. Souma, *Phys. Rev. B* **73**, 075303 (2006).

¹⁶ The ratio $t_R/|U|$ is of the order of 10^{-3} (Ref. 6) to 10^{-2} (Ref. 7) for graphene, and of 10^{-1} for $\text{Bi}(111)$ bilayer surfaces (Ref. 9 and 10). The reported value in $\text{Ti/Si}(111)-(1 \times 1)$ surface alloy (Ref. 3) leads to an even stronger ratio $t_R/|U| \sim 0.4$.